1-1-2010

The Zeeman Effect in the Sobolev Approximation II. Radial Split Monopole Fields and the 'Heartbeat' Stokes V Profile.

K. Gayley
University of Iowa

Richard Ignace
East Tennessee State University

The Zeeman Effect in the Sobolev Approximation II. Radial Split Monopole Fields and the 'Heartbeat' Stokes V Profile.

THE ZEEMAN EFFECT IN THE SOBOLEV APPROXIMATION: SPLIT MONOPOLE FIELDS AND THE "HEARTBEAT" STOKES V PROFILE

K. G. GAYLEY[1] AND R. IGNACE[2]
[1] Department of Physics and Astronomy, University of Iowa, Iowa City, IA 52245, USA
[2] Department of Physics and Astronomy, East Tennessee State University, Johnson City, TN 37663, USA

ABSTRACT

We calculate the circularly polarized Stokes $V(\lambda)$ profile for emission lines, formed in hot-star winds threaded with a weak radial magnetic field. For simplicity, the field is treated as a split monopole under the assumptions that it has been radially combed by the wind, and rotation is not playing a central role. Invoking the weak-field approximation, we find that the $V(\lambda)$ profile has a characteristic "heartbeat" shape exhibiting multiple sign inversions, which might be mistaken for noise in the absence of theoretical guidance. We also conclude that there is a tendency for the $V(\lambda)$ profile to integrate to zero on each side of the line separately. The overall scale of $V(\lambda)/I(\lambda)$ is set by the ratio of the field strength to the flow speed, B/v, characteristic of the line-forming region, and is of the order of 0.1% for a wind magnetic field $B \cong 100\,G$ at depths where the wind speed is $v \cong 100$ km s^{-1}.

Key words: line: profiles – polarization – radiative transfer – stars: magnetic fields – stars: winds, outflows

1. INTRODUCTION

Recent advances in spectropolarimetry have ushered in a new era of detecting and characterizing the surface magnetic fields of hot stars (e.g., Donati et al. 1997, 2006; Bouret et al. 2008; Hubrig et al. 2008; Wade et al. 2009). What still lies ahead is extending these results into the winds, where the magnetic fields can have an important dynamical influence. Indeed, magnetic fields of optically thick winds, like those of Wolf–Rayet stars, cannot be seen in the static layers owing to shrouding by the supersonic wind.

In some instances, new detections come when pre-existing observations are subject to closer theoretical scrutiny. In others, theory can *lead* and *motivate* observations, guiding the detections of signals that might otherwise be too weak to distinguish confidently from noise. It is this latter goal of theoretical support that motivates the approach of this paper, and as a result we adopt a rough and exploratory treatment of the line formation and magnetic environment.

As the detection of weak ($\lesssim$100 G) fields is the goal here, it seems likely that such fields will be combed out into a nearly radial configuration for strong-wind stars, perhaps transitioning into a spiral pattern at larger radii where the flow time approaches the rotation period (Friend & MacGregor 1984; Ignace et al. 1998). Although pockets of locally elevated magnetic fields may lead to a different class of field detections in the wind, here we explore the more generic case of a smooth, global, and largely radial field, using a split monopole field to grossly represent this general configuration. Hence our goal is to determine the characteristic circular polarization signature of a recombination line formed in a strong wind with a split monopole magnetic field, and to use that prediction to assist observers in making detections if such generic fields exist, given that the first detections will likely be a challenge to distinguish from noise. We leave the issue of highly asymmetric structures to future work.

The reason that direct diagnostics of radial fields would be of value is that they have dynamical importance whenever the local Alfven speed approaches the local wind speed. Thus they are important when

$$1 \lesssim \frac{B}{\sqrt{4\pi\rho}\,v} \cong \frac{B}{111\ \text{G}}\ \frac{r}{10\,R_\odot}\ \left(\frac{v}{100\ \text{km s}^{-1}}\right)^{-1/2}$$
$$\times \left(\frac{\dot{M}}{10^{-5}\ M_\odot\ \text{yr}^{-1}}\right)^{-1/2}, \tag{1}$$

where B is the magnetic field and $\dot{M}$ is the mass-loss rate. Apparently, for the wind speeds of interest in supersonic winds, $\gtrsim$100 km s^{-1}, there is dynamical significance when $B \gtrsim 100$ G. Open fields with B substantially in excess of 100 G would likely leave a conspicuous imprint on the stellar spindown time (MacGregor et al. 1992; ud-Doula et al. 2009), but the impact of somewhat weaker fields would be more difficult to interpret, and a more direct diagnostic of their presence is sought.

1.1. The Weak-Field Approximation

Throughout we adopt the weak-field approximation (Landi Degl'Innocenti & Landi Degl'Innocenti 1972; Jefferies et al. 1989), whereby the longitudinal Zeeman shift and the circular polarization act as though they were responding to a magnetic field that was purely the line-of-sight component of the actual field. Taking our wavelength scale x (measured from line center) to be in units of the Doppler shift of a fiducial velocity v_1, designed to be flexible to the context of interest, then the contribution to the Stokes V parameter for some infinitesimal region with a given magnetic field $\vec{B}$ and without regard for any velocity gradient (that is, not invoking the Sobolev approximation) is

$$dV(x) = \frac{dI(x + \Delta x) - dI(x - \Delta x)}{2}, \tag{2}$$

where $dI(x)/2$ is the contribution to the specific intensity in either polarization in the absence of any B field. Here

$$\Delta x = \frac{\Delta\lambda_B}{\lambda_o}\frac{c}{v_1} = \frac{\vec{B}\cdot\hat{n}}{v_1}\xi_o \tag{3}$$

determines the wavelength shift for a line-of-sight magnetic field $\vec{B} \cdot \hat{n}$, so it determines the modification to the $dI(x)$ in each polarization. Also, λ_o is the wavelength of the line, and

$$\Delta\lambda_B = 1.4 \times 10^{-3} \,\text{Å} \, g_{\text{eff}} \frac{\vec{B} \cdot \hat{n}}{100 \,\text{G}} \left(\frac{\lambda_o}{5500 \,\text{Å}}\right)^2 \qquad (4)$$

is the longitudinal Zeeman shift. The constant ξ_o depends only on line parameters, specifically the effective Lande factor g_{eff} and the line wavelength λ_o, and is given by

$$\xi_o = 7.7 \times 10^{-4} \, g_{\text{eff}} \left(\frac{\lambda_o}{5500 \,\text{Å}}\right) \frac{\text{km s}^{-1}}{\text{G}}. \qquad (5)$$

At this stage v_1 is arbitrarily chosen, but our convention for Δx and x will be to use for v_1 a fiducial wind speed at the zone of peak line formation, a point which we term $r = 1$ because we also scale the radius to this point. This flexible approach allows the actual value of x and Δx to be interpreted from the shape of the line profile itself, rather than requiring independently specified physical scales. Note that the above expressions merely serve to describe the action of the weak-field approximation and the role of the Zeeman shift; below we will add the assumption of a steep velocity gradient and apply the Sobolev approximation, modifying Equation (2) to account for the interplay between the velocity v gradient and the B gradient.

The weak-field approximation applies for fields whose Zeeman shift, expressed in units of velocity, is much smaller than the characteristic broadening velocity of the profile. For unresolved surface fields, that is the rotational velocity of the star, but for winds, it is the wind speed v_1 characteristic of the line formation. The latter can be much faster, and indeed our neglect of rotation requires that it is. Such wind speeds are extremely large on the scale of the Zeeman effect, since a 100 G magnetic field produces Zeeman shifts of only about 1 km s^{-1} in optical lines, and this justifies the use of the weak-field approximation. As such, our focus is not on strong-field stars like Ap/Bp stars (e.g., Babel & Montmerle 1997; Townsend & Owocki 2005), wherein the presence of multi-kG magnetic fields leaves a rigid imprint on the circumstellar dynamics. Instead, we are interested in magnetic fields that are closer to equipartition with the wind kinetic energy, where the field dynamical importance is more subtle, but for detectable fields, would still be important to understand.

This approximation allows for an especially powerful conceptual convenience in the context of *radial* fields, because then the line-of-sight component of the B field depends on angle in the same way as does the line-of-sight component of the wind speed v (also assumed radial). As such, the Zeeman shift has an effect that closely mimics the Doppler shift, but with different sign in the two polarizations. Then the presence of a radial B field serves as a kind of polarization-dependent modification to the effective wind velocity law, for purposes of line diagnostics. Subtracting the intensity profiles from these effectively different wind velocity laws then gives the Stokes flux profile $V(x)$.

1.2. Previous Results

This project was begun in Ignace & Gayley (2003), where some conclusions were reached about the expected overall scale of the polarization, and the prospects for detection in the winds of $\sim$100 G fields seemed challenging, but potentially possible with current technology. However, that analysis included only

what we term here the "gradient effect," whereby the Zeeman shifts imply that the contributing volume at a given wavelength penetrates to slightly lower r in one circular polarization than in the other, an effect related to why the $I(x)$ profile slopes downward as $|x|$ increases. However, the current paper will elucidate an additional equally important effect, the "binning effect," which accounts for the fact that a given wavelength bin, integrated over emission in all directions, will receive contribution over a *smaller solid angle* for whichever polarization has a Zeeman shift that *augments* the Doppler shift. Or looked at in an equivalent way, the Zeeman shifts for that polarization would cause emission into the same solid angle to be stretched over a wider wavelength bin, by augmenting the Doppler effect.

When the binning effect is appropriately included, we show here that optically thin recombination lines should be expected to have their Stokes $V(x)$ signal cancel out when integrated over wavelength on either side of the line, red *or* blue. This does not imply that the entire $V(x)$ profile cancels, however, because the positive and negative components are somewhat separated in frequency, and the good spectral resolution that is standard in modern spectropolarimetry can resolve the positive from the negative contributions if sufficient care is taken. Nevertheless, the presence of multiple inversions in the sign of the polarization suggests that knowing what spectral shape in $V(x)$ to expect may be helpful in distinguishing a real signal from noise.

Also, for optically *thick* lines, we will explore here two new effects that also modify the Stokes $V(x)$ profile, which both have to do with the fact that magnetized optically thick lines in the Sobolev approximation have different escape probabilities, from the local Sobolev zone, in different directions for the different polarizations. The new effect we term the "angle effect" stems from the fact that for a given observed wavelength, the two different circular polarizations must escape their Sobolev zones along different angles to appear at the same observed wavelength, and that can favor the escape of one polarization over the other. The other new effect we term the "shape effect," whereby the gradient in the Zeeman shift alters the Doppler gradient that sets the shape of the Sobolev zone, augmenting escape in some directions and reducing it in others. This latter effect assists the escape of photons when the field gradient augments the velocity gradient, and hinders escape when they offset, and that can also favor one polarization over the other.

As we shall see, accounting for these three new effects, one in thin lines and two more in thick, does not generally alter the overall *scale* of the circular polarization, but does alter its detailed spectral *signature*. It is hoped that knowing in advance what signature to look for will help observers disentangle what is noise from what is signal, at least in the generic context of a split-monopole field treatment.

2. STOKES V WITH RADIAL B FIELDS FOR OPTICALLY THIN LINES

Let us first consider the case of optically thin lines (so photons created in the line escape the Sobolev zone without scattering). Here only one additional effect needs to be added to Ignace & Gayley (2003), the "binning effect." Below we show that the binning effect produces an opposite net circular polarization to the gradient effect, and this signal appears closer to line center, so the two together yield a characteristic "heartbeat" signature in $V(x)/I(x)$ that exhibits one sign inversion in each profile wing and one more at the line center.

2.1. Basic Definitions

As we are ultimately interested only in the ratio V/I and its profile shape, we can scale both the wavelength x (from line center) and the radius r by their characteristic values at the region of peak line formation. Thus $r = 1$ is typically the photospheric radius (either at the stellar surface or at the wind photosphere for thick winds, and we include no emission from $r < 1$), and $x = 1$ is typically the wavelength that resonates at $r = 1$, which might appear as an edge of a "flat top" for profiles with a broad peak, or more generally as a kind of half-width at half-maximum for more rounded profiles. It is not necessary to be more specific, because the scaling of both x and r are arbitrary to within a constant factor—it is only the shape and magnitude of $V(x)/I(x)$ that we need to understand, and the shape of the $I(x)$ profile itself defines the operational meaning of x.

What is actually measured for an unresolved point source is the flux density (per wavelength bin and per detector area) $F(x)$, but this includes an inverse-square dependence on the distance D to the source, which is not a variable of interest here. We remove that dependence, and also simplify the appearance of factors of π later on, by defining

$$I(x) = \frac{D^2}{\pi} F(x). \tag{6}$$

Then $V(x)$ is defined by decomposing $I(x)$ into its contributions from opposite circular polarizations, and subtracting the left-hand $(-)$ from the right-hand $(+)$ components.

We also need to specify the tight connection between wavelength x and radius r, enforced by the Sobolev approximation in the presence of steep v gradients that allow us to neglect thermal motions in comparison to the bulk motion, and allow us to neglect interactions in any other regions outside the wind photosphere. That connection is controlled by the combined Doppler and Zeeman shifts along the direction cosine μ between the observer and the gas parcel in question. The result for each of the + and – circular polarizations, using Equation (3) for weak fields, is

$$x_\pm = -v(r)(1 \mp b)\mu, \tag{7}$$

where $v(r)$ is the velocity scaled to the wind speed at $r = 1$ (and corresponding to $\mu = 1$ and $x = 1$ if magnetic fields are neglected), and

$$b(r) = 7.7 \times 10^{-4} g_{\text{eff}} \left(\frac{\lambda_o}{5500\,\text{Å}} \right) \left(\frac{B(r)}{100\,\text{G}} \right) \left(\frac{v(r)}{100\,\text{km s}^{-1}} \right)^{-1} \tag{8}$$

comes from Equation (3). Note that when B measured in G equals v measured in km s^{-1}, the numerical value of ξ_o gives b. Since ξ_o depends only on the line in question, lines with larger ξ_o generate larger $b(r)$ and are more favorable for detecting circular polarization. The overall magnitude of b is set by B/v, and this determines the detectability of the signal.

The sign conventions used are that v is regarded as positive for radially outward flow, and B is regarded as positive for radially outward field, so b is positive for radially outward $\vec{B}$ also. This means that a split monopole field, for a given polarization, has b augmenting the effective v in the hemisphere where $\vec{B}$ is radially outward, and reducing it in the hemisphere where $\vec{B}$ is radially inward. The "+" polarization for $V(x)$ is right circular, and this is always listed as the upper sign when two signs are present. We will always assume $|b| \ll 1$ and work only to lowest nonvanishing order, consistent with the weak-field approximation.

Another important function is the derivative $d\mu/dx_\pm$, which controls the width of the solid-angular slice at each emitting point that will contribute in the dx wavelength bin in each polarization. Thus $d\mu/dx_\pm$ controls the binning of the emission (and results in the binning effect), and is given by

$$\left| \frac{d\mu}{dx_\pm} \right| = \frac{1 \pm b(r)}{v(r)}. \tag{9}$$

It is apparent that when $b > 0$, so for radially outward $\vec{B}$, right-hand circular polarization experiences Zeeman shifts that enhance the Doppler effect and spread the emission from a given solid angle over a wider wavelength bin. This in turn tends to yield a negative $V(x)$, and oppositely for radially inward $\vec{B}$.

Finally, we will assume throughout the paper that there exists a known line emissivity function $j(r)$, the rate of creation of radiant energy in the line per volume per solid angle (assuming isotropic creation) at radius r, in either of the two independent circular polarizations (recall that the weak-field approximation to the longitudinal Zeeman effect treats all emission as circularly polarized, and the local creation rate in the two polarizations is indistinguishable). Further, we assume that known emissivity is of power-law form,

$$j(r) = j_o r^{-p}. \tag{10}$$

Here p may be treated as a variable to treat various types of emission mechanisms, escape probabilities, ionization degrees, and velocity laws.

Since $j(r)$ is per volume, the radial integrand for the emission scales as r^{2-p}, and we assume $p > 3$ and carry the integration to $r = \infty$. The neglect of any dependence of photon creation rate on polarization is a reflection of the fact that the Zeeman shift relative to the line wavelength, $\Delta\lambda_B/\lambda_o$, is smaller than the scale of b by the factor $v/c \sim 10^{-3}$. Hence the effects of b, which redistribute polarized emission over the line, appear long before the effects of any real difference in the creation rate of photons in the two polarizations.

2.2. The Unipolar Field Result V^*

Since the interest here is in radial B fields and radial v flows, a great simplification is offered by adopting spherical symmetry. The main stumbling block in using spherical symmetry with magnetic fields is, of course, that a strictly spherically symmetric field must be monopolar, so we may conclude that any physically attainable field must break spherical symmetry. However, by choosing a *split* monopole field for our study, we preserve the maximal symmetry consistent with zero magnetic divergence, since a split monopole field is constructed from a spherically symmetric monopole field by reversing the field throughout one hemisphere.

Because of the close connection between split monopole fields and fields that are truly spherically symmetric (and hence unphysical), it is actually convenient to first calculate the Stokes $V(x)$, which we denote $V^*(x)$, that corresponds to a hypothetical spherically symmetric field. Despite being strictly unphysical, this approach will be seen to have pedagogical value, and in the case when $V^*(x)$ corresponds to a monopole field (i.e., $B \propto 1/r^2$), it can be mapped to the split monopole result after the fact, just by accounting manually for the hemispheric field reversal. Furthermore, in this paper we consider only the most favorable case where the observer sees the star along one magnetic pole, and then mapping $V^*(x)$ into $V(x)$ is as trivial as reversing its sign on one whole side of line center.

These considerations allow us to compute $V(x)$ from the $V^*(x)$ in complete spherical symmetry, which is a helpful simplification. Specifically, it allows the line profile to be calculated using a single integral over radius, because the emission in each radial bin dr maps into each dx bin according only to the solid-angle fraction established by $d\mu/dx$, where μ is the direction cosine to *any hypothetical observer* that would be in position to detect that emission. Normally we would only be interested in a *particular* observer, but due to the complete spherical symmetry, we can count all emission as being detected by an array of equivalent observers in all directions, and merely divide by the solid angle of any particular detector to find the actual observed profile flux. Indeed, since we are ultimately interested only in the comparison $V^*(x)/I(x)$, there is no need for the final step, as we may just as well count all emission as observed emission.

Carrying out the radial integral for the wind emission, and for simplicity ignoring occultation and any photospheric continuum effects (hence we are picturing fairly strong emission lines), the results may be written as

$$I(x) = \int_{r_+(x)}^{\infty} dr\, r^2 j(r) \left| \frac{d\mu}{dx} \right|_+ + \int_{r_-(x)}^{\infty} dr\, r^2 j(r) \left| \frac{d\mu}{dx} \right|_- \quad (11)$$

and

$$V^*(x) = \int_{r_+(x)}^{\infty} dr\, r^2 j(r) \left| \frac{d\mu}{dx} \right|_+ - \int_{r_-(x)}^{\infty} dr\, r^2 j(r) \left| \frac{d\mu}{dx} \right|_-, \quad (12)$$

where $r_\pm(x)$ is the formation depth in each polarization for emission in the outward radial direction at x. That is, $r_\pm(x)$ solves $x = v(r_\pm)[1 \mp b(r_\pm)]$, and since we envision all emission as coming from $r > 1$, whenever we would otherwise have $r_\pm(x) < 1$ we replace $r_\pm$ with unity. Also, since we are working only to lowest nonvanishing order in b, there is no need to include any magnetic effects in the calculation of $I(x)$, so for that calculation $r_\pm = r_\pm(B = 0) = \bar{r}(x)$ comes from $v(\bar{r}) = x$, and we take $b_\pm = 0$.

Finally, for pole-on observing of a purely radial field that switches from outward in one hemisphere to inward in the other, we have $V(x) = V^*(x)x/|x|$. For other observing angles, there will be some intra-hemispheric cancellation that is straightforward to compute by also carrying out the azimuthal integrations that our current symmetry assumptions allow us to suppress. For this analysis, we are interested in establishing the maximum detectability threshold for a radial field, so we adopt the most optimistic assumption of pole-on observing, and this also simplifies the mapping from $V^*(x)$ to $V(x)$.

2.3. Heuristic "Heartbeat" Signal for $B \propto v$

To advance our understanding of the desired diagnostic signature, we again imagine complete spherical symmetry and move in a pedagogically useful but even more physically impossible direction, by considering $B \propto v$. Such a situation not only violates the global divergence-free constraint, it even shows *local* divergence whenever v induces density changes, as for spherically diverging supersonic winds. But for schematic purposes, this assumption has the useful characteristic that here the Zeeman shift will be in *constant proportion* to the Doppler shift, except with opposite sign in the two polarizations (see Equation (8)).

Hence for optically thin lines, the two polarizations will act *exactly* like two winds with $v(r)$ rescaled by $1 \mp b_o$, where b_o

is a global constant. Such a rescaling has the effect of rescaling the x axis of the profile by this same global factor, and rescaling the intensity axis by the inverse amount (as the total emission in the two polarizations is conserved when the lines are thin enough to avoid polarization redistribution during escape). It is this extremely simple behavior that motivates our schematic assumption.

Hence in this case, direct examination of the $I(x)$ profile for that line would immediately allow us to compute $V^*(x)$:

$$V^*(x) = \frac{1}{2} \{(1 + b_o)I[(1 + b_o)x] - (1 - b_o)I[(1 - b_o)x]\}. \quad (13)$$

To lowest order in b_o, this gives

$$\frac{V^*(x)}{I(x)} = b_o \left[1 + \frac{d \ln I}{d \ln x} \right] \quad (14)$$

and for pole-on observers, changing sign in the rear hemisphere ($x < 0$) gives

$$\frac{V(x)}{I(x)} = b_o \frac{x}{|x|} \left[1 + \frac{d \ln I}{d \ln x} \right]. \quad (15)$$

For a generally bell-shaped $I(x)$ profile, this would produce the results as illustrated in Figure 1, for $b_o = 10^{-3}$ (other b_o values would generate a proportional scaling). Although a physically unimportant case, the pedagogical value of $B \propto v$ is that it provides an immediate way to see the *qualitative* attributes of the $V(x)$ profile for radial B fields, given only knowledge of $I(x)$ and b_o, and it suggests a useful form for expressing the more quantitative results that follow for a more physically plausible field treatment. Specifically, we are introduced to the overall "heartbeat" shape, while the general form of Equation (15) explicitly demonstrates the "binning" (first term) and "gradient" (second term) effects.

2.4. The Split Monopole Results

The simplest physically possible radial B field configuration is the split monopole, for which $B = \pm B_1 r^{-2}$ (where the "1" subscript refers to the value at $r = 1$), with a positive sign (outward) in one hemisphere and a negative sign (inward) in the other. To determine $b(r)$, we need to specify $v(r)$, and here we take the homologous approximation $v = r$, simulating lines that form in the heart of the acceleration region, neither close to nor far from the static star. Again the physical scale of v and r are arbitrary because we are interested only in the shape of the $V(x)$ profile relative to the shape of the $I(x)$ profile.
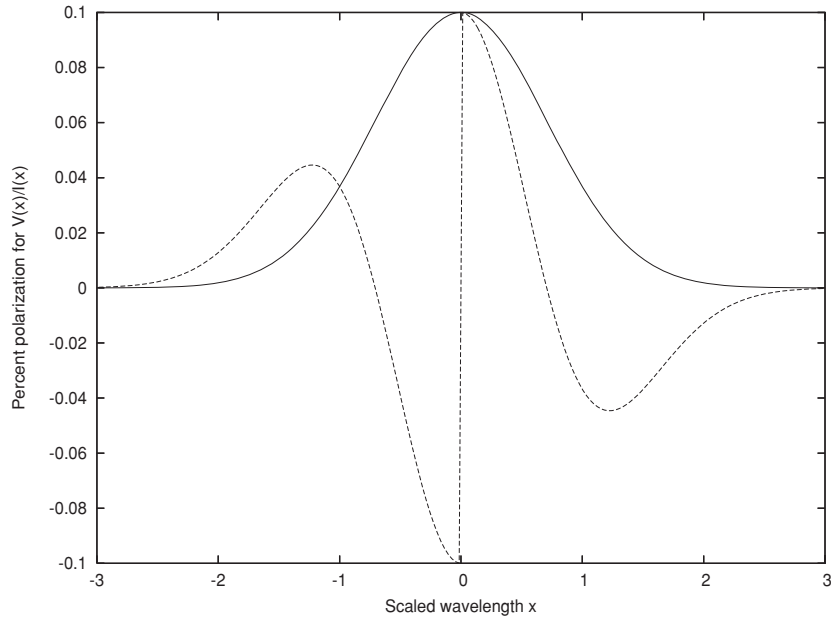
When we assume homologous expansion, $v = r$, we have $b(r) = b_1 r^{-3}$, and Equations (11) and (12) produce

$$\frac{V^*(x)}{I(x)} = \frac{\int_{r_+}^{\infty} dr\, r^{1-n}(1 + b_1 r^{-3}) - \int_{r_-}^{\infty} dr\, r^{1-n}(1 - b_1 r^{-3})}{2 \int_{\bar{r}}^{\infty} dr\, r^{1-n}}. \quad (16)$$

Then for $|x| > 1$ we have for the minimum radius of formation of the two polarizations for wavelength x

$$r_\pm(x) = x \mp \frac{b_1}{x^2} \quad (17)$$

and $\bar{r}(x) = x$, and for $|x| < 1$ we have $r_\pm(x) = \bar{r}(x) = 1$, as we neglect line emission inside $r < 1$ to simulate a photosphere

Figure 1. Percent polarization (dashed curve) of $V(x)/I(x)$ for a heuristic Gaussian profile with a constant $b = 10^{-3}$, so B is everywhere proportional to the radial velocity v, and reverses polarity in one hemisphere, for a pole-on observer. Although this would only be physically possible for an incompressible velocity field, it shows the qualitative attributes of the circular polarization for an optically thin line. $I(x)$ in arbitrary units is also shown (solid curve) to clarify the meaning of the x scale.

or an ionization change. Carrying out the elementary integrals yields for $|x| < 1$

$$\frac{V^*(x)}{I(x)} = \frac{(p-2)}{(p+1)} b_1 \tag{18}$$

for

$$I(x) = \frac{1}{(p-2)} \tag{19}$$

and for $|x| > 1$

$$\frac{V^*(x)}{I(x)} = -\frac{p(p-2)}{(p+1)} b_1 x^{-3} \tag{20}$$

for

$$I(x) = \frac{x^{-(p-2)}}{(p-2)}. \tag{21}$$

Here the scale of $I(x)$ is arbitrary but its shape defines the meaning of the x scale. It has a flat top in this case, because we assume a sharp cutoff in the line formation at $r = 1$, but only its general shape is relevant to the discussion. Here a simple recombination line of a majority species with $v = r$ would correspond to $p = 6$. The results for $I(x)$ and $V(x)/I(x)$ for pole-on inclination with $n = 4, 5$, and 6 are shown in Figure 2.

2.5. A General Expression for V*(x)/I(x) for Thin Lines

A useful way to express Equation (16) is to place it in a form similar to Equation (14). Working to lowest order in b gives for $|x| > 1$

$$\frac{V^*(x)}{I(x)} = \langle b \rangle_x + b(x) \frac{d \ln I}{d \ln x}, \tag{22}$$

where $b(x)$ is $b(r)$ evaluated at $r = \bar{r}(x)$, and $\langle b \rangle_x$ is an average value given by

$$\langle b \rangle_x = \frac{\int_{\bar{r}}^{\infty} dr \, r^2 \, \frac{j(r)}{v(r)} b(r)}{\int_{\bar{r}}^{\infty} dr \, r^2 \, \frac{j(r)}{v(r)}}. \tag{23}$$

Note that in the heuristic case $b = b_o$ from Equation (14), we have $\langle b \rangle_x = b(x) = b_o$. When $v = r$ and $b(r) = b_1 r^{-3}$, we have $\langle b \rangle_x = b_1(n-2)/(n+1)$ and $d \ln I/d \ln x = 0$ for $|x| < 1$ where the radial integrals are from $r = 1$ to $r = \infty$, and when $|x| > 1$, the radial integrals are from $r = x$ to $r = \infty$, and $\langle b \rangle_x = b_1(p-2)/(p+1)x^3$ and $d \ln I/d \ln x = 2 - p$. For split monopole fields, $b(x) = b_1/x^3$, and the generalized form recovers the same results as above.

Specifically, the new form shows that $V(x)$ receives contribution from a term that depends on $I(x)$ itself, and a term that depends on the slope of $I(x)$. The term that is proportional to $I(x)$ stems from the "binning" effect, whereby for a given x, a polarization whose Zeeman shifts augment the Doppler shift has its intensity weakened by being spread over more frequency bins, and the term that depends on the slope of $I(x)$ stems from the "gradient" effect, whereby a polarization whose Zeeman shift augments the Doppler shift originates from deeper depths so receives contribution from a larger volume. The opposing signs of these two contributions suggest they tend to cancel when *integrated* over either side of the emission profile, and we next explore the simple reason why this integrated cancellation is indeed complete for thin lines.

2.6. A Line-Integrated Constraint on V(x) for Optically Thin Lines

Since we consider radial fields and radial flows, and since $v = 1$ is considered to be already highly supersonic, the Zeeman shift in the weak-field approximation does not pass any emission across line center, so the forward hemisphere maps into the blue side of the line and the reverse hemisphere into the red. Then the fact that for optically thin lines, the total emission in each polarization is the same in any volume implies that $\int_0^{\infty} dx \, V(x) = 0$ when integrated over either side of the line. Seeing this feature in $V(x)$ profiles (as it continues to hold *approximately* for optically thick lines as well) would be a good indication of the presence of approximately radial fields, and
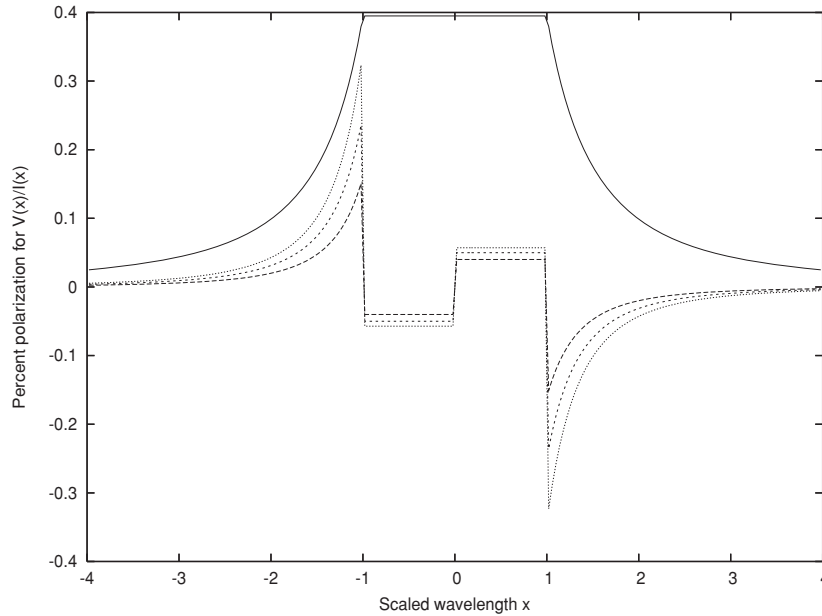
Figure 2. Percent polarization of $V(x)/I(x)$ for a thin line with power-law emissivity where $b_1 = 10^{-3}$ at the deepest formation depth of the line, for a split monopole field and a pole-on observer. The different curves are for emissivity power laws $p = 4$, 5, and 6, where the larger p yield the larger percent polarization, as the steeper emissivity powers imply that more of the emission comes from closer to the deepest formation depth $r = 1$, where B/v is larger. Flat-topped $I(x)$ in arbitrary units is also shown (solid curve), to show the meaning of the x scale.

it underscores the need for good spectral resolution to see not only the usual Zeeman-type overall line asymmetry, but also a polarization reversal on *each side* of the line independently, which is the general characteristic of the "heartbeat" feature.

Note that it is not $V(x)/I(x)$ that integrates to zero—the core portion of the percent polarization tends to be diluted by the bright core of $I(x)$, so $V(x)/I(x)$ would tend to show more clearly the polarization in the wings of $I(x)$. Hence the sign of the wing polarization would dominate if it were $V(x)/I(x)$ that was being integrated over x, as suggested in Figure 2.

3. STOKES V WITH RADIAL B FIELDS FOR OPTICALLY THICK LINES

When the Sobolev optical depth in the line obeys $\tau_S \gg 1$, photons created in the line must locally scatter until they are able to escape from resonance, in the familiar ways inherent in the Sobolev approximation. This introduces two new avenues for imprinting a net polarization into the profile that we will analyze next, in the context of a complete redistribution approximation.

3.1. Complete Redistribution in Angle, Wavelength, and Polarization

Optically thick line scattering is vastly simplified by assuming that enough scatterings occur such that all "memory" of the initial wavelength (within the line), angle, and polarization of the newly created photon is rapidly lost prior to escape from the Sobolev zone. One may then assume that each scattering is like a new creation event for that photon, independent of its history. This approximation has a generally good reputation in optically thick environments, though its spectacularly streamlining properties are the main reason it is used. We will make the same approximation here to take advantage of that simplification, and an investigation of the errors introduced is beyond the scope of this initial investigation into the general detectability of weak radial B fields.

### 3.2. The Angular Escape Probability

The fundamental new complication that appears for thick lines is that the shape of the emergent intensity profile depends not only on the radius-dependent photon creation rate, but also on the angle-dependent escape probability from the Sobolev zones. In complete frequency redistribution, the Sobolev escape probability when $\tau_S \gg 1$ is inversely proportional to the Sobolev optical depth τ_S, along the direction μ from Equation (7). All we require is the *relative* escape probability $\beta(r, \mu)$ because we are treating only the *effectively thin* situation where all photons created in the line escape in the line, so the relative escape probability can be normalized to unity when integrated over escaping μ. The Zeeman shift changes this normalized relative escape probability to lowest order in $b(r)$ into

$$\beta_\pm(r, \mu) = \frac{1 + \sigma_v \mu^2 \mp b(r)\left(1 + \sigma_b \mu^2\right)}{1 + \sigma_v/3 \mp b(r)(1 + \sigma_b/3)}, \qquad (24)$$

where $\sigma_v = (d \ln v/d \ln r) - 1$ and $\sigma_b = (d \ln B/d \ln r) - 1$ control the line-of-sight Doppler and Zeeman shifts along μ. For $v = r$, $\sigma_v = 0$, and for split monopole fields, $\sigma_b = -3$.

As noted above, $\beta_\pm$ is normalized so that $\int_{-1}^{1} d\mu \, \beta_\pm = 1$, as it is a relative photon escape probability normalized over the (assumed isotropic) creation and scattering of photons in the line. It already assumes an angular escape profile inversely proportional to the optical depth profile, so applies only to lines that are optically thick to scattering, and its normalization further requires that the line be effectively thin in the sense that all photons created in the line eventually escape in the line. Effectively *thick* lines would not be ideal candidates for observing $V(x)/I(x)$, because they would likely form too far out in the wind where B/v is low, so would dilute the $V(x)$ signal against a bright and largely unpolarized $I(x)$ profile.
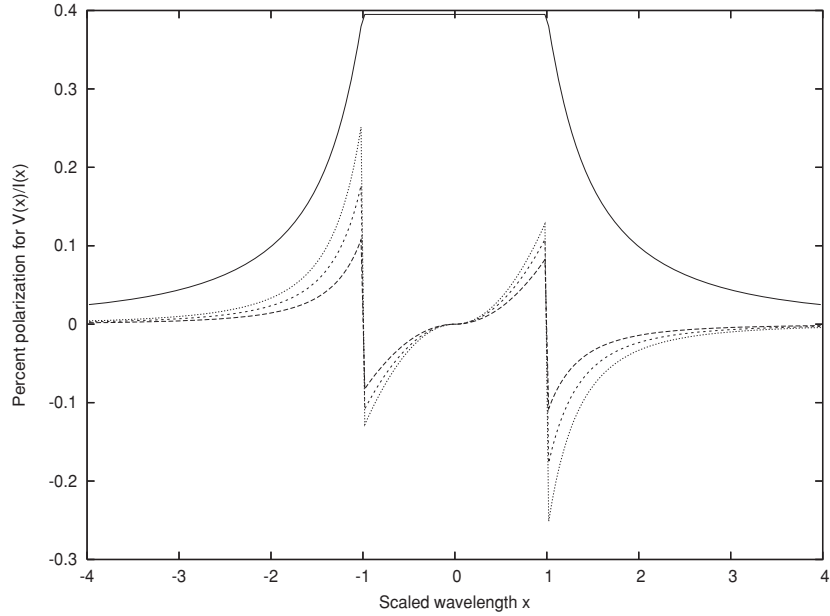
Figure 3. Percent polarization of $V(x)/I(x)$ for a thick line with power-law emissivity where $b_1 = 10^{-3}$ at the deepest formation depth of the line, for a split monopole field and a pole-on observer. The different curves are for emissivity power laws $p = 4$, 5, and 6, where the larger p yield the larger percent polarization just as in Figure 2. Also shown (solid curve) is the flat-topped $I(x)$ in arbitrary units, which again defines the meaning of the x scale.

3.3. The Split Monopole Results

Integrating the wind emission, and ignoring occultation and any photospheric continuum effects for simplicity, optically thick but effectively thin lines yield the same *eventual* escape as optically thin lines (i.e., unity), so without Zeeman influences they yield the same $I(x)$ as in Equation (11). However, to lowest order in b we do have changes to $V(x)$ given by

$$V^*(x) = \int_{r_+(x)}^{\infty} dr \, r^2 j(r) \left| \frac{d\mu}{dx} \right|_+ \beta_+(r, x)$$
$$- \int_{r_-(x)}^{\infty} dr \, r^2 j(r) \left| \frac{d\mu}{dx} \right|_- \beta_-(r, x) \qquad (25)$$

where the product

$$\left| \frac{d\mu}{dx} \right|_{\pm} \beta_{\pm} = \frac{\left(1 + \sigma_v \frac{x^2}{v^2}\right)}{\left(1 + \frac{\sigma_v}{3}\right)v} \left[1 \pm \frac{3b(1 + \sigma_v)\frac{x^2}{v^2}}{\left(1 + \sigma_v \frac{x^2}{v^2}\right)} \right] \qquad (26)$$

is expanded to first order in b, using $\sigma_b = -3$. Again v and b in these expressions are evaluated at the $r_{\pm}(x)$ that solves Equation (7) for $\mu = 1$, and since we treat all emission as coming from $r > 1$, whenever we would otherwise have $r_{\pm}(x) < 1$ we replace $r_{\pm}$ with unity.

If we again take $v = r$ to treat lines that form in the heart of the acceleration region where the expansion is approximately homologous, we have $\sigma_v = 0$ and $b(r) = b_1 r^{-3}$, then Equation (26) gives

$$\left| \frac{d\mu}{dx} \right|_{\pm} \beta_{\pm} = \frac{1}{r} \left(1 \pm 3b_1 \frac{x^2}{r^5} \right) \qquad (27)$$

and Equations (11) and (12) now become

$$\frac{V^*(x)}{I(x)} =$$
$$\frac{\int_{r_+(x)}^{\infty} dr \, r^{1-p}(1 + 3b_1 x^2 r^{-5}) - \int_{r_-(x)}^{\infty} dr \, r^{1-p}(1 - 3b_1 x^2 r^{-5})}{2 \int_{\bar{r}(x)}^{\infty} dr \, r^{1-p}}.$$
$$(28)$$

Then for $|x| > 1$ we again have

$$r_{\pm}(x) = x \mp \frac{b_1}{x^2} \qquad (29)$$

and $\bar{r}(x) = 1$, and for $|x| < 1$ we have $r_{\pm}(x) = \bar{r}(x) = 1$. The integrals yield for $|x| < 1$

$$\frac{V^*(x)}{I(x)} = \frac{3(p-2)}{(p+3)}b_1 x^2 \qquad (30)$$

with

$$I(x) = \frac{1}{(p-2)}. \qquad (31)$$

For $|x| > 1$, we obtain

$$\frac{V^*(x)}{I(x)} = -\frac{p(p-2)}{(p+3)}b_1 x^{-3} \qquad (32)$$

with

$$I(x) = \frac{x^{-(p-2)}}{(p-2)}. \qquad (33)$$

Note that the results for $I(x)$ are identical in the thick and thin cases, because when $v = r$ the escape from the Sobolev zone is isotropic either way, and we are treating only the effectively thin situation where all line photons, once created, will escape before being rethermalized. The results for $I(x)$ and $V(x)/I(x)$ for pole-on inclination and $p = 4$, 5, and 6 are shown in Figure 3.

3.4. The General Form for $V^*(x)/I(x)$ for Thick Lines with $v = r$

The purpose of this investigation is to seek *general* aspects of the circular polarization profile due to weak radial fields, and as such the specific shape of the $I(x)$ and the $V(x)$ profiles are not the primary concern, but rather the connection *between* them. What are the attributes of the $I(x)$, given $b(x)$, that contribute to generating a detectable $V(x)/I(x)$ polarized fraction? To

address this for thick lines, we may again place Equation (28) in a form similar to Equation (14), except that now

$$\frac{V^*(x)}{I(x)} = 3x^2 \left\langle \frac{b}{v^2} \right\rangle_x + b(x) \frac{d \ln I}{d \ln x}, \qquad (34)$$

where again $b(x)$ is $b(r)$ evaluated at $r = \bar{r}(x)$, and $\langle f \rangle_x$ is the same emission average as in the thin case. If we then take $v = r$ and $b(x) = b_1 x^{-3}$, we have for $|x| < 1$ that $3x^2 \langle b/v^2 \rangle_x = 3(p-2)b_1 x^2/(p+3)$ and $d \ln I/d \ln x = 0$, recovering $V^*(x)/I(x) = -3(p-2)b_1 x^2/(p+3)$. For $|x| > 1$, we have $3x^2 \langle b/v^2 \rangle_x = 3(p-2)b_1 x^2/(p+3)$ and $d \ln I/d \ln x = 2 - p$, so $V^*(x)/I(x) = -p(p-2)b_1 x^{-3}/(p+3)$ as above.

4. DISCUSSION

The above results show that for thin lines, the $V^*(x)$ profile integrates to zero over either side of line center, but this constraint is no longer satisfied by thick lines, because Zeeman shifts may actually favor the net escape of the polarization that effectively augments the velocity gradient and enhances escape in that polarization. However, the overall "heartbeat" shape appears for both thick and thin lines, so there is still polarization reversal on each side of the line, and the potential exists for cancellation if the wavelength scale of the inversion is not resolved. The inversion should appear somewhere near where the slope in $I(x)$ is maximal, so observational techniques that co-add bins to increase signal must exert caution in that vicinity, lest the bins so generated be too wide and enhance cancellation. Careful inspection of the signal near sign reversals is thus advisable, if global radial fields are present.

One caveat in regard to the problem of unintentional polarization cancellation should be noted. Our schematic approach of choosing a sharp cutoff in the line formation at $r = 1$ is related to the profile kink that separates the core and wings of $I(x)$, and this kink is also associated with the discontinuous spike in the wing polarization seen in Figures 2 and 3. This spiky behavior in the wings of $V(x)$ is not seen in Figure 1, because there is no sharp cutoff involved in the line formation that is implicit in that figure. Hence, we may conclude that the sharp and discontinuous wing spike is an artifact of our treatment, and a smoother transition is to be expected, unless the $I(x)$ profile itself transitions abruptly from flat-topped to sloping downward. A smoother transition would also involve some cancellation near the discontinuity in our spiky results, so one should not interpret the peak polarization at the spikes as being real or observationally attainable. Nevertheless, the sign transition is the feature of interest, and the capacity to resolve that feature should inform the choices made when co-adding bins.

Our results show that discontinuities in $V(x)$ can also appear at line center, as in the unphysical situation seen in Figure 1 where the magnitude of $B(r)$ is proportional to $v(r)$ (but has a polarity inversion like the split monopole), and also for optically thin lines with a split monopole field as in Figure 2. In realistic models, the line of magnetic polarity inversion would not appear strictly in the hemisphere perpendicular to the line of sight to the star, so the polarization inversion would be more gradual than we depict, but nevertheless could be very noticeable. A gradual transition with little polarization near line center, on the other hand, happens for optically thick lines with homologous expansion as in Figure 3, because then Zeeman influences near line center ($x = 0$) experience a compensation between the "binning effect" (regulated by $d\mu/dx$) and the "shape effect"

(regulated by β), as seen in Equation (26), which causes $V^*(x)$ to tend to zero as x does (like x^2, we find). This in turn causes $V(x)$ to pass not only continuously through zero at line center, but also with zero slope, in contrast to the sharp transition in thin lines. Note the "gradient effect" and the "angle effect" are not active near line center, so thin lines experience only the binning effect there, whereas thick lines experience both the binning effect and the shape effect, affecting the rate of escape along $\mu = 0$ into the dx bin.

The more generic situation is that of Figures 1 and 2, where a sharp transition is seen—the delicate cancellation that produces Figure 3 is a more specialized behavior, although of course some smoothing of the transition will occur due to any non-ideal aspects of the magnetic geometry and inclination. Because of this, we suggest that whenever observations show a polarization signal that tends sharply through zero as it crosses line center, observers should not discount the possibility of a detection of a real signal *near* line center.

The behavior of the polarization near line center, its magnitude and the sharpness of the sign inversion, may thus be useful in distinguishing thick from thin lines, and homologous expansion from other forms. For example, the shape of $I(x)$ itself would not suffice to distinguish thick and thin lines under homologous expansion, because then $I(x)$ has identical shape whenever the lines are effectively thin, regardless of whether or not they are optically thin, because the escape from the Sobolev zone is isotropic in either case.

Our most robust results, which depend the least on our model assumptions, is the general form of Equations (22) and (34). These show how the shape of $I(x)$ is dependent on the shape of $V(x)$, in the most flexible terms possible, for thin and thick lines respectively, for split monopole fields seen pole-on. In that situation, these expressions can actually be used to invert the $V(x)$ and $I(x)$ profiles into an effective $b(x)$ distribution, and thereby probe the $v(r)$ profile assuming a monopolar $B(r)$.

Even more generally, these points suggest that for any type of polarization detection, considerations involving the underlying field topology and global wind model may dictate the effectiveness of various data analysis strategies, and mapping that connection motivates theoretical studies of other types of field geometries in future. This may be particularly relevant in light of the reported detection by Donati et al. (2005) of circularly polarized lines in the disk of FU Ori, demonstrating the capability to detect the longitudinal Zeeman effect in circumstellar environments at a sub-percent degree of polarization.

All our results, even those for optically thick lines, assume that the lines are *effectively* thin, so all photons created in the line escape in the line. It should be noted that when this is not the case, the $I(x)$ will drop relative to what our expressions give, but the $V(x)$ will drop *even more*, since $V(x)$ forms at the greater depths where B/v is largest, but that is also where the lines would be the most effectively thick and rethermalization would be most severe. This would have to be seen against an unfortunately bright background of $I(x)$ that forms farther out, where the wind is less dense and rethermalization is less of a problem, and would be largely unpolarized due to the rapidly dropping B/v. Hence it is suggested that effectively thick lines are to be avoided, despite yielding very bright emission lines, because the presence of many photons is not always a benefit when they serve only to dilute the polarized component.

Similarly, emission lines that are too weak would be diluted by unpolarized continuum emission, which we did not include in this study to maintain our focus on strong lines with maximum

simplicity. Hence it is suggested that lines of intermediate strength, with peak intensities about as bright as the continuum, and significant emission from regions in the wind moving considerably slower than 1000 km s^{-1}, would be best suited for detecting global radial fields. Lines with larger values of the ξ_o parameter are also favored.

5. SUMMARY AND CONCLUSIONS

Figures 2 and 3, and Equations (22) and (34), present the fundamental results of this paper, that the circular polarization profile $V(x)/I(x)$ for a split monopole field should exhibit a characteristic "heartbeat" shape, explained heuristically in Figure 1. The scale of the circular polarization is determined by the b parameter, so by the ratio B/v characteristic of the peak line formation region, and we find the peak signal in $V(x)/I(x)$ reaches as high as $p(p-2)/(p+1)$ times b_1 for thin lines, and around $p(p-2)/(p+3)$ times b_1 for thick lines. Here p is the power-law index in the volume emissivity, and $p \cong 6$ for the recombination of the dominant species in a region of nearly homologous expansion. Thus $V(x)/I(x)$ might be expected to peak at a level of nearly $3b_1$, although this may be somewhat optimistic because of smoothing mechanisms that would create some cancellation in the sharpest spikes in $V(x)$. It was stated earlier that $b_1 \sim 8 \times 10^{-4} g_{\text{eff}}$ at 5500 Å, when $B = 100$ G and $v = 100$ km s^{-1} are characteristic of the peak line-forming region designated $r = 1$, manifested in the profile near $x \cong 1$ where the wings of $I(x)$ begin to fall steeply. Hence it would not be surprising if a local B field of 100 G at a wind photosphere at 100 km s^{-1} can yield a peak $V(x)/I(x)$ polarization at the 0.1% level under ideal conditions. Inversely, the greatest challenge to the detection of fields at the 100 G level is if the dominant contribution to the line emission comes at radii where the wind is substantially faster than 100 km s^{-1}.

All these appear to show promise that fields strong enough to have any dynamical significance in hot-star winds may lie within the reach of modern instrumental detectability, and it is our hope that these results will help assist observers in making detections of such fields if they do in fact exist. We find it especially significant that the Stokes V signature, owing to the Doppler shifts of rapidly approaching and receding wind hemispheres, reverses sign once on each side of the profile, rather than doing so only at line center where Stokes V profiles normally reverse in static photospheric applications. This gives observers a morphological constraint to look for which might otherwise be mistaken for noise were it not expected from the theory. Sharp inversions across line center are also possible and would be as diagnostically useful as inversions in the wings. The potential presence of multiple sign changes in the polarized spectrum is a potentially important issue to bear in mind when binning data to increase signal.

Rotational modulation of the $V(x)/I(x)$ signal would also help separate signal from noise, if the magnetic axis misaligns with the rotation axis, because such a misalignment would create a periodic variation in the inclination of the magnetic pole. If the fields are not seen pole-on, the conversion from $V^*(x)$ to $V(x)$ must include partial cancellation between the side lobes toward and away from the direction of tilt of the magnetic pole, owing to the reversal in the magnetic polarity across the neutral line of radial fields. Hence the results given here are more fundamentally interpreted as a calculation of the spherically symmetric template $V^*(x)$, with the determination of the observed $V(x)$ following from geometric considerations of the (possibly varying) inclination of the magnetic neutral line. Here we consider only the ideal configuration to constrain detectability under the most optimistic conditions—clearly, the most pessimistic conditions would include a viewing angle along the magnetic equator, resulting in complete cancellation of the circular polarization at all wavelengths, unless the field is highly asymmetric.

We stress that the split monopolar configuration is chosen here simply to exemplify a field with a high degree of symmetry, and because of its "generic" character in a dense radial wind environment. These seem like more natural assumptions for guiding observations, than would making detailed fits to specific conditions intended to match observations that do not currently exist. Although theoretical considerations suggest that when rotation is unimportant, approximately radial fields might thread dense winds, there remain ample opportunities for real winds to deviate from quasi-spherical symmetry, especially when rotation *is* dynamically important. For example, evidence for such symmetry breaking is present in the rapidly rotating WR star EZ CMa (St-Louis et al. 1995; Morel et al. 1998), so it is certainly possible that magnetic detections in hot-star winds may result from aspherical pockets of intense emission from structures in the wind, rather than from the smooth radial fields considered here. Only future observations can resolve this point.

Our current analysis has not considered stellar occultation or emission from the stellar photosphere, as we have envisioned fairly strong recombination lines for whom photospheric occultation and emission would not dominate the wind emission. Neither would it be negligible, however, unless the lines are very strong, but as we have seen, such lines would likely form too far out to be ideal for $V(x)/I(x)$ detections in a weak global B field. Thus, for important lines of interest, circular polarization from the red wing may well be reduced by occultation, and from the blue wing may be diluted somewhat by the photospheric continuum. Our results are therefore not yet at the level of direct modeling of observed profiles, such detailed modeling is better attempted once promising observational detections already exist.

Also, our simple model does not account for clumping, despite significant evidence that clumping is prevalent in hot-star winds (Hillier et al. 2003; Zsargo et al. 2008). But since our approach is sensitive to the radial distribution of j but not its overall magnitude, only radially varying emission enhancements due to clumping would have an impact. Any such radial dependence could be treated as a straightforward modification to the power law in j, which is one of the reasons we parameterized the emissivity in a fairly general way. Since clumping that did not affect the B field would tend to affect $I(x)$ and $V(x)$ similarly, it would likely not have a significant impact on the degree of polarization. However, depending on the dynamics of the clumping process, it might engender a local increase in B, increasing the field detectability in pockets where the emission is especially strong. These are viewed as quantitative details that must be considered at the level of profile fitting once the basic effects are detected.

Besides these issues, it will also be important to expand our approaches to other geometries. Already, we have made an initial attempt at predicting the V profile from a Keplerian disk (Ignace & Gayley 2008). Further explorations of disks and extensions to rigidly corotating structures (e.g., relevant to Ap/Bp stars like σ Ori E, Townsend et al. 2005) will be pursued in the future.

REFERENCES

Babel, J., & Montmerle, T. 1997, A&A, 323, 121
Bouret, J.-C., Donati, J.-F., Martins, F., Escolano, C., Marcolino, W., Lanz, T., & Howarth, I. D. 2008, MNRAS, 389, 75
Donati, J.-F., Paletou, F., Bouvier, J., & Ferreira, J. 2005, Nature, 438, 466
Donati, J.-F., Semel, M., Carter, B. D., Rees, D. E., & Collier Cameron, A. 1997, MNRAS, 291, 658
Donati, J.-F., et al. 2006, MNRAS, 370, 629
Friend, D. B., & MacGregor, K. B. 1984, ApJ, 282, 591
Hillier, D. J., Lanz, T., Heap, S. R., Hubeny, I., Smith, L. J., Evans, C. J., Lennon, D. J., & Bouret, J. C. 2003, ApJ, 588, 1039
Hubrig, S., Schöller, M., Schnerr, R. S., Gonzalez, J. F., Ignace, R., & Henrichs, H. F. 2008, A&A, 490, 793
Ignace, R., Cassinelli, J. P., & Bjorkman, J. E. 1998, ApJ, 505, 910
Ignace, R., & Gayley, K. G. 2003, MNRAS, 341, 179
Ignace, R., & Gayley, K. G. 2008, in Clumping in Hot-Star Winds, ed. W.-R. Hamann, A. Feldmeier, & L. M. Oskinova, 137
Jefferies, J., Lites, B. W., & Skumanich, A. 1989, ApJ, 343, 902
Landi Degl'Innocenti, E., & Landi Degl'Innocenti, M. 1972, Sol. Phys., 27, 319
MacGregor, K. B., Friend, D. B., & Gilliland, R. L. 1992, A&A, 256, 141
Morel, T. S., Moffat, A. F. J., Cardona, O., Koenigsberger, G., & Hill, G. M. 1998, ApJ, 498, 413
St-Louis, N., Dalton, M. J., Marchenko, S. V., Moffat, A. F. J., & Willis, A. J. 1995, ApJ, 452, 57
Townsend, R. H. D., & Owocki, S. P. 2005, MNRAS, 357, 251
Townsend, R. H. D., Owocki, S. P., & Groote, D. 2005, ApJ, 630, 81
ud-Doula, A., Owocki, S. P., & Townsend, R. H. D. 2009, MNRAS, 392, 1022
Wade, G. A., et al. 2009, in IAU Symp. 259, Cosmic Magnetic Fields: From Planets, to Stars and Galaxies, ed. K. G. Strassmeier, A. G. Kosovichev, & J. E. Beckman (Dordrecht: Kluwer), 333
Zsargo, J., Hillier, D. J., Bouret, J.-C., Lanz, T., Leutenegger, M. A., & Cohen, D. H. 2008, ApJ, 685, 149